J. Fluid Mech. (2013), *vol.* 714, *pp.* 312–335. © Cambridge University Press 2013
doi:10.1017/jfm.2012.483

Coupled oscillations of deformable spherical-cap droplets. Part 1. Inviscid motions

J. B. Bostwick[1,2] **and P. H. Steen**[2,3,†]

[1]Department of Mathematics, North Carolina State University, Raleigh, NC 27695, USA
[2]Department of Theoretical & Applied Mechanics, Cornell University, Ithaca, NY 14853, USA
[3]School of Chemical and Biomolecular Engineering and Center for Applied Mathematics, Cornell University, Ithaca, NY 14853, USA

(Received 6 April 2012; revised 2 August 2012; accepted 27 September 2012)

A spherical drop is constrained by a solid support arranged as a latitudinal belt. This belt support splits the drop into two deformable spherical caps. The edges of the support are given by lower and upper latitudes yielding a 'spherical belt' of prescribed extent and position: a two-parameter family of constraints. This is a belt-constrained Rayleigh drop. In this paper we study the linear oscillations of the two coupled spherical-cap surfaces in the inviscid case, and the viscous case is studied in Part 2 (Bostwick & Steen, *J. Fluid Mech.*, vol. 714, 2013, pp. 336–360), restricting to deformations symmetric about the axis of constraint symmetry. The integro-differential boundary-value problem governing the interface deformation is formulated as a functional eigenvalue problem on linear operators and reduced to a truncated set of algebraic equations using a Rayleigh–Ritz procedure on a constrained function space. This formalism allows mode shapes with different contact angles at the edges of the solid support, as observed in experiment, and readily generalizes to accommodate viscous motions (Part 2). Eigenvalues are mapped in the plane of constraints to reveal where near-multiplicities occur. The full problem is then approximated as two coupled harmonic oscillators by introducing a volume-exchange constraint. The approximation yields eigenvalue crossings and allows post-identification of mass and spring constants for the oscillators.

Key words: bubble dynamics, capillary flows, drops

1. Introduction

Liquid drops held by surface tension are known to assume spherical equilibrium shapes. When perturbed, the inviscid drop will oscillate at small amplitude with the characteristic frequency and mode shape given by Lord Rayleigh (1879). The Rayleigh oscillating drop, of undisturbed radius R, which will be alternatively referred to as the 'unconstrained oscillator', has frequencies ordered in a discrete spectrum

$$\omega_n^2 = \frac{n(n-1)(n+1)(n+2)}{(n+1)\rho_i + n\rho_e}\frac{\sigma}{R^3}, \quad n = 0, 1, \ldots, \tag{1.1}$$

---

† Email address for correspondence: phs7@cornell.edu

where σ is the surface tension and ρ_i and ρ_e are the densities of the interior and exterior fluids, respectively. Corresponding mode shapes have radial deformations that are given by the Legendre polynomials, $P_n(\cos\theta)$. These theoretical results have been verified experimentally for immiscible drops by Trinh & Wang (1982) and for free drops in microgravity by Wang, Anilkumar & Lee (1996).

The Rayleigh problem has been extended by Strani & Sabetta (1984, 1988) to vibrations of a constrained spherical drop, where the constraint forms a solid support of spherical bowl shape. In this case, the undisturbed state is a single spherical cap. We shall refer to this problem as the 'Strani oscillator'. Strani oscillator predictions have also compared favourably to experiment (Bisch, Lasek & Rodot 1982; Trinh, Zwern & Wang 1982; Rodot & Bisch 1984). We extend to two coupled spherical caps. A new feature is that the free-surface domains are disconnected. In contrast to the Strani approach, ours accommodates two disconnected domains and is immediately generalizable to three or more domains. From the applied side, our study is motivated by the growing interest in the dynamics of capillary systems.

The motions of constrained drops are of interest in a number of emerging applications. Examples include drop atomization (James, Smith & Glezer 2003*a*; James *et al.* 2003*b*; Vukasinovic, Smith & Glezer 2007), switchable electronically controlled capillary adhesion (Vogel, Ehrhard & Steen 2005; Vogel & Steen 2010) and optical microlens devices (Lopez, Lee & Hirsa 2005; Lopez & Hirsa 2008; Olles *et al.* 2011). The last two are rooted in the idea of the capillary switch (Bhandar & Steen 2005; Hirsa *et al.* 2005; Theisen *et al.* 2007; Malouin, Vogel & Hirsa 2010). The capillary switch is composed of two disjoint interfaces which are allowed to communicate (coupled) through the underlying fluid, much like the communication that occurs for the belted-sphere. Of interest for coating processes and microfluidic applications is the control of droplet motion induced by means of a harmonically driven substrate (Daniel *et al.* 2004; Noblin, Buguin & Brochard-Wyart 2004, 2005; Noblin, Kofman & Celestini 2009; Brunet, Eggers & Deegan 2009). In these studies, a deformable drop is constrained by the substrate on which the droplet rests.

In this paper, we study the linear stability of two coupled spherical-cap surfaces made by constraining a spherical drop with a solid support (see figure 1 below). The solid support conforms to the spherical surface and extends between two latitudes, $\theta_2 \leqslant \theta \leqslant \theta_1$, forming a 'spherical belt'. The resulting free surface consists of two spherical caps (disconnected) which are coupled through the liquid beneath (connected). The interfaces are pinned at the edges of the belt and their motion is governed by integro-differential equations. The perspective is set by the question: To what extent can the resultant motions be understood as those of coupled harmonic oscillators? In the inviscid case, the unconstrained limit recovers the Rayleigh drop problem.

In the constrained problem, the interface is the union of a surface of support and two independent free surfaces, which are coupled by the underlying pressure field through the incompressibility condition. The two surfaces oscillate with a frequency that can be sensitive to the extent and position of the belt constraint, depending on the values (θ_1, θ_2). Near-multiplicities occur when two different modes oscillate at nearly the same frequency. When there are near-multiplicities, the system is prone to significant nonlinear interactions (Tsamopoulos & Brown 1983; Hammack & Henderson 1993). Hence, knowing where such near-multiplicities occur in the plane of constraints is important to applications. We identify these near-crossings, or 'pinch points', in a plot of frequency against constraint. Alternatively, pinch points are observed to correlate with the volume displaced by one surface of the two pinching

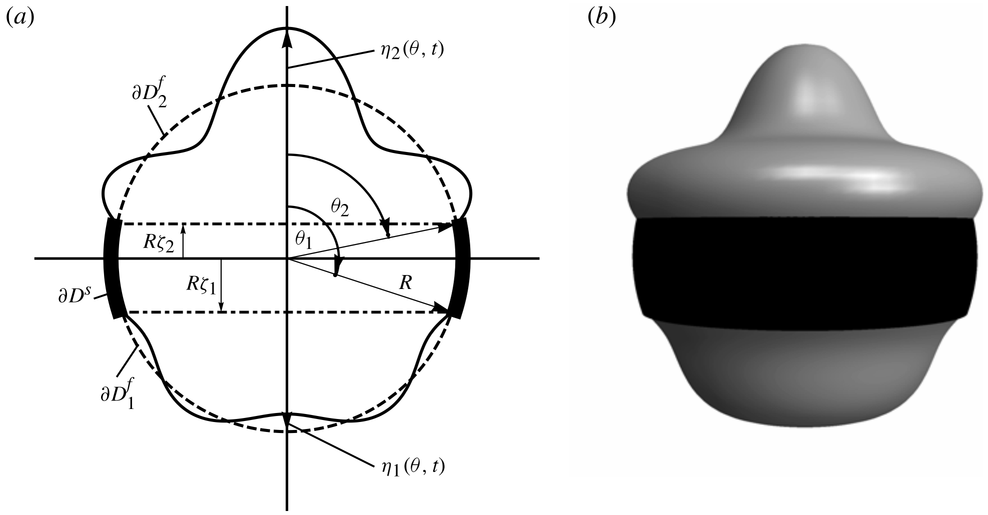

FIGURE 1. (*a*) Definition sketch in two-dimensional polar view and (*b*) sample deformation in three-dimensional perspective view. Disturbances η_1 and η_2 are constrained by the belt support extending over $\zeta_1 \equiv \cos\theta_1 \leqslant \cos\theta \leqslant \zeta_2 \equiv \cos\theta_2$. Lengths ζ are scaled by R while lengths η are left unscaled.

modes. This observation provides a physical characterization of the near-multiplicities and a method for identifying them.

Finally, motivated by the volume-exchange observations, we introduce the approximation of two Strani-like oscillators. Each oscillator is characterized by the volume displaced. The coupling between these linear oscillators occurs via an average pressure arising as the Lagrange multiplier for the displaced-volume constraint. The coupled Strani-like oscillator approximation is compared to the exact solution and is found to be an effective tool for identifying frequency crossings. Finally, solutions of the coupled Strani-like oscillator operator equations can be reduced to finite-dimensional mass–spring oscillators by identification of effective-mass and -spring constants. This is a post-processing step.

To study drop motion in the absence of base-state symmetry, one generally turns to a computationally based method. Finite-element methods have been employed to study the finite-amplitude natural oscillations of pendant drops (Basaran & DePaoli 1994), as well as the forced oscillations of supported drops with application to drop ejection (Wilkes & Basaran 2001) and hysteretic response (Wilkes & Basaran 1999), which was reported experimentally by DePaoli *et al.* (1995). More recently, Ramalingam & Basaran (2010) have analysed the forced oscillations of the double droplet system (DDS) by various types of excitation. In another numerical study, James *et al.* (2003*a*) developed a Navier–Stokes solver to capture the drop ejection phenomenon of forced sessile drops.

A number of papers consider motions of drops constrained by either planar or spherical-like supports. For drops in contact with a planar support, Gañan & Barerro (1990) focus on the pinned contact-line disturbance. More recently, attention has been paid to more general wetting conditions and dynamics of the three-phase contact line (Lyubimov, Lyubimova & Shklyaev 2004, 2006; Fayzrakhmanova & Straube 2009). Exploiting symmetry, Lyubimov *et al.* (2006) have investigated the free and forced axisymmetric oscillations of an inviscid hemispherical drop, whose contact-line motion is prescribed by a linearized Hocking condition relating the contact angle to the contact-line speed. A similar analysis is given for asymmetric disturbances by Lyubimov *et al.* (2004). Fayzrakhmanova & Straube (2009) implement the full Hocking condition via numerical integration to study the stick–slip dynamics and frequency response caused by contact-angle hysteresis of the forced hemispherical drop.

For drops in contact with a spherical-bowl constraint, the works of Strani & Sabetta (1984, 1988), Bauer & Chiba (2004) and Theisen *et al.* (2007) are most relevant to this study. Strani & Sabetta (1984) consider the linear oscillations of an inviscid drop in contact with a 'spherical bowl' by using a Green's function approach to derive an integral eigenvalue equation, which is then reduced to a set of linear algebraic equations by a Legendre series expansion. They report a low-frequency mode, not present for isolated drops. Furthermore, the eigenfrequencies are shown to grow as the spherical-bowl support is increased from the single point of contact to the fully enclosed sphere. Strani & Sabetta (1988) extend their inviscid analysis to the viscous case. Our study recovers the results of these studies. Bauer & Chiba (2004, 2005) have also investigated spherical 'bowl-like' constraints for captured inviscid and viscous drops by approximating finite-sized constraints with a large number of point-wise constraints. Theisen *et al.* (2007) study moderate-amplitude coupled oscillations of non-deformable spherical caps – two drops pinned on circle of contacts at either end of a tube – and report centre-of-mass motions. When compared to their experiments, the spherical-cap approximation is reasonably accurate for these low-frequency drop–drop oscillations. However, for certain initial disturbances, higher-order mode shapes are excited. To model these higher-order mode shapes, Bostwick & Steen (2009) analysed the linear oscillations of a deformable drop constrained by a latitudinal circle of contact and report a shift in the characteristic frequencies compared to the unconstrained drop, including the low-frequency $n = 1$ mode. Their analysis utilizes a 'Rayleigh–Ritz procedure and assumes continuous derivatives (contact angles) as well as a continuous displacement across the circle-of-contact constraint. Observations from droplet–droplet experiments suggest discontinuous contact angles, however (see Bostwick & Steen 2009, figure 10). In the formulation in this paper, derivatives of displacement need not be continuous across the belt constraint.

We begin this paper by defining the linearized field equations and relevant boundary conditions from which the equation of motion for the drop interface is derived and formulated as an eigenvalue problem on linear operators. The operator eigenvalue equation is reduced to a truncated set of linear algebraic equations using a Rayleigh–Ritz procedure on a constrained function space. The eigenvalues/modes, which depend upon relative densities and the geometry of the constraint, are then computed. We compare these solutions to various approximations in the appropriate limits. Next, the problem is reformulated as two coupled oscillators using the exchange volume as an embedding parameter. This reduction is particularly effective in identifying eigenvalue near-multiplicities in the plane of constraints, which are found to correlate with the exchange volume. We conclude with some remarks on the computational results.

2. Mathematical formulation

Consider an unperturbed spherical droplet of radius R, constrained by a spherical belt given through the polar angle $\theta_2 \leqslant \theta \leqslant \theta_1$ in spherical coordinates (r, θ), as shown in the definition sketch (figure 1). The drop interface is disturbed by time-dependent free-surface perturbations, $\eta_1(\theta, t)$ and $\eta_2(\theta, t)$, which are assumed to be axisymmetric and small. No domain perturbation is needed for linear problems, thus the domain is the combination of the regions internal to and external to the static droplet:

$$D^i \equiv \{(r, \theta) \mid 0 < r \leqslant R, 0 \leqslant \theta \leqslant \pi\}, \qquad (2.1a)$$

$$D^e \equiv \{(r, \theta) \mid, R < r < \infty, 0 \leqslant \theta \leqslant \pi\}. \qquad (2.1b)$$

The interface separating the interior and exterior fluids (internal boundary) is given by the union of two free surfaces and one surface of support:

$$\partial D_1^f \equiv \{(r, \theta) \mid r = R, \theta_1 \leqslant \theta \leqslant \pi\}, \qquad (2.2a)$$

$$\partial D_2^f \equiv \{(r, \theta) \mid r = R, 0 \leqslant \theta \leqslant \theta_2\}, \qquad (2.2b)$$

$$\partial D^s \equiv \{(r, \theta) \mid r = R, \theta_2 \leqslant \theta \leqslant \theta_1\}, \qquad (2.2c)$$

$$\partial D \equiv \partial D_1^f \cup \partial D_2^f \cup \partial D^s. \qquad (2.2d)$$

The interior and exterior fluids are assumed to be inviscid, incompressible and immiscible. The effect of gravity is neglected.

2.1. *Field equations*

The velocity field for this irrotational flow can be written as $\boldsymbol{u} = -\nabla\Psi$, where the velocity potential Ψ satisfies Laplace's equation,

$$\nabla^2\Psi = \frac{\partial}{\partial r}\left(r^2\frac{\partial\Psi}{\partial r}\right) + \frac{1}{\sin\theta}\frac{\partial}{\partial\theta}\left(\sin\theta\frac{\partial\Psi}{\partial\theta}\right) = 0 \quad [D^i, D^e], \qquad (2.3)$$

in both interior (i) and exterior (e) sub-domains, as required by fluid incompressibility. The pressure field for small interface disturbances is given by the linearized Bernoulli equation,

$$P = \rho\frac{\partial\Psi}{\partial t} \quad [D^i, D^e]. \qquad (2.4)$$

Henceforth, to distinguish between sub-domains, subscripts will be used to denote material properties and superscripts for field quantities, such as density $\rho_{i,e}$ and pressure $P^{i,e}$, respectively.

2.2. *Boundary/integral conditions*

The no-penetration condition requires a vanishing radial velocity at the surface of support,

$$\frac{\partial\Psi}{\partial r} = 0 \quad [\partial D^s], \qquad (2.5)$$

whereas the linearized kinematic condition relates the normal velocities of the fluid and free-surface deformation there,

$$\frac{\partial\Psi}{\partial r} = -\frac{\partial\eta_{1,2}}{\partial t} \quad [\partial D_1^f, \partial D_2^f]. \qquad (2.6)$$

The difference in pressures across the interface is balanced by the surface tension σ times the linearized mean curvature of the disturbed surface,

$$P^i - P^e = -\frac{\sigma}{R^2}\left(\frac{1}{\sin\theta}\frac{\partial}{\partial\theta}\left(\sin\theta\frac{\partial\eta_{1,2}}{\partial\theta}\right) + 2\eta_{1,2}\right) \quad [\partial D_1^f, \partial D_2^f]. \qquad (2.7)$$

Lastly, the integral form of the incompressibility condition (volume conservation) constrains the free-surface disturbances to satisfy

$$\int_{\theta_1}^{\pi} \eta_1(\theta, t) \sin\theta \, \mathrm{d}\theta + \int_{0}^{\theta_2} \eta_2(\theta, t) \sin\theta \, \mathrm{d}\theta = 0. \tag{2.8}$$

Note that (2.3)–(2.8) are the linearized disturbance equations.

2.3. *Normal-mode reduction*

Normal modes

$$\Psi(r, \theta, t) = \phi(r, x)\mathrm{e}^{\mathrm{i}\omega t}, \quad P(r, \theta, t) = p(r, x)\mathrm{e}^{\mathrm{i}\omega t}, \quad \eta_{1,2}(\theta, t) = y_{1,2}(x)\mathrm{e}^{\mathrm{i}\omega t}, \tag{2.9}$$

with $x \equiv \cos\theta$, are applied to the governing hydrodynamic equations (2.3)–(2.8) to yield the following boundary-value problem on the reduced functions ϕ and y_1, y_2:

$$\nabla^2\phi = \frac{\partial}{\partial r}\left(r^2\frac{\partial\phi}{\partial r}\right) + \frac{\partial}{\partial x}\left((1-x^2)\frac{\partial\phi}{\partial x}\right) = 0 \quad [D^i, D^e], \tag{2.10a}$$

$$\frac{\partial\phi}{\partial r} = 0 \quad [\partial D^s], \tag{2.10b}$$

$$\frac{\partial\phi}{\partial r} = -\mathrm{i}\omega y_{1,2}(x) \quad [\partial D_1^f, \partial D_2^f], \tag{2.10c}$$

$$p = \mathrm{i}\omega\rho\phi \quad [D^i, D^e], \tag{2.10d}$$

$$p^i - p^e = -\frac{\sigma}{R^2}\left(\frac{\partial}{\partial x}\left((1-x^2)\frac{\partial y_{1,2}}{\partial x}\right) + 2y_{1,2}\right) \quad [\partial D_1^f, \partial D_2^f], \tag{2.10e}$$

$$\int_{-1}^{\zeta_1} y_1(x)\,\mathrm{d}x + \int_{\zeta_2}^{1} y_2(x)\,\mathrm{d}x = 0. \tag{2.10f}$$

Equations (2.10) define an eigenvalue problem for the oscillation frequency ω. Here the shape parameters

$$\zeta_1 \equiv \cos(\theta_1), \quad \zeta_2 \equiv \cos(\theta_2), \tag{2.11}$$

define the geometry of the spherical-belt constraint.

3. Reduction to an operator equation

The eigenvalue problem (2.10) is reduced to an integro-differential equation in this section. The resulting equation governs the motion of the interface and is formulated as an eigenvalue equation on linear operators.

3.1. *Velocity potential solution*

A general solution to the boundary-value problem (2.10*a*)–(2.10*c*) for the velocity potential ϕ is sought. To begin, consider boundary conditions (2.10*b*) and (2.10*c*) as a single boundary condition on the interface (2.2*d*) and restrict ‘allowable’ interface disturbances to have the form

$$y(x) = \begin{cases} y_1(x), & -1 \leqslant x \leqslant \zeta_1, \\ 0, & \zeta_1 \leqslant x \leqslant \zeta_2, \\ y_2(x), & \zeta_2 \leqslant x \leqslant 1. \end{cases} \tag{3.1}$$

The solution to (2.10*a*)–(2.10*c*) is then given by (e.g. Arfken & Weber 2001)

$$\phi^i(r,x) = -\mathrm{i}\omega R \sum_{k=1}^{\infty} \frac{d_k}{k}\left(\frac{r}{R}\right)^k P_k(x), \tag{3.2a}$$

$$\phi^e(r,x) = \mathrm{i}\omega R \sum_{k=1}^{\infty} \frac{d_k}{k+1}\left(\frac{R}{r}\right)^{k+1} P_k(x), \tag{3.2b}$$

where

$$d_k \equiv \frac{(y, P_k)}{(P_k, P_k)}. \tag{3.3}$$

Here P_k is the Legendre polynomial of degree k and (f, g) is the inner product of square integrable functions on the domain $x \in (-1, 1)$,

$$(f, g) = \int_{-1}^{1} f(x)g(x)\,\mathrm{d}x. \tag{3.4}$$

3.2. *Integro-differential equation*

We now scale interface deformation y, $y \equiv Ry^*$, and drop the * for notational simplicity in what follows. The balance of capillary pressure (2.10*e*) and inertial pressure (2.10*d*), evaluated at the drop surface using the velocity potential solution (3.2), generates an integro-differential equation governing allowable deformations,

$$(1-x^2)y_{xx} - 2xy_x + 2y = -\lambda^2\left[\sum_{k=1}^{\infty}\left(\frac{1}{k} + \frac{\rho_e}{\rho_i}\frac{1}{k+1}\right) d_k P_k(x)\right]. \tag{3.5}$$

Here $\lambda^2 \equiv \rho_i\omega^2 R^3/\sigma$ is the scaled frequency. The interface deformation y must satisfy the following boundary/integral conditions:

$$y(\pm 1) - \text{bounded}, \tag{3.6a}$$

$$\int_{-1}^{1} y(x)\,\mathrm{d}x = 0, \tag{3.6b}$$

$$y(\zeta_1 \leqslant x \leqslant \zeta_2) = 0. \tag{3.6c}$$

Equation (3.6*a*) is a necessary condition to guarantee that the interface deformation is physical, while (3.6*b*) follows directly from the conservation-of-volume constraint (2.10*f*). Lastly, the no-penetration condition on the surface of support is satisfied by (3.6*c*).

3.3. *Operator equation*

To solve the eigenvalue problem (3.5) and (3.6), it is instructive to formulate the integro-differential equation as an operator equation

$$\lambda^2 M[y] + K[y] = 0, \tag{3.7}$$

where

$$M\left[y; \frac{\rho_e}{\rho_i}\right] \equiv \sum_{k=1}^{\infty}\left(\frac{1}{k} + \frac{\rho_e}{\rho_i}\frac{1}{k+1}\right)\left(\frac{2k+1}{2}\right)\left(\int_{-1}^{1} y P_k\,\mathrm{d}x\right) P_k(x) \tag{3.8}$$

is a positive-definite integral operator, the density ratio ρ_e/ρ_i is a material parameter and

$$K[y] \equiv (1-x^2)\frac{\mathrm{d}^2 y}{\mathrm{d}x^2} - 2x\frac{\mathrm{d}y}{\mathrm{d}x} + 2y \tag{3.9}$$

is a self-adjoint differential operator. Putting $y = P_n(x)$ in (3.7) recovers the spectrum (1.1).

4. Solution of the operator equation

The frequency spectrum and corresponding mode shapes of the eigenvalue equation (3.7) are computed using the variational procedure of Rayleigh–Ritz. The necessary input to such a procedure is a predetermined function space, which is constructed to satisfy the no-penetration condition on the surface of support and to couple the independent free-surface perturbations, y_1 and y_2, according to the incompressibility condition (2.10*f*). Equivalently, the two free surfaces are allowed to 'communicate' across the spherical-belt constraint through the underlying fluid, subject to the conservation-of-volume constraint. The eigenfrequencies/modes are computed using standard numerical routines from a truncated set of linear algebraic equations, which results from application of the variational procedure.

4.1. *The Rayleigh–Ritz method*

The eigenvalue equation (3.7) is posed as a variational one, using Rayleigh–Ritz formalism, whereby the eigenvalues are computed by minimizing the following functional:

$$\lambda^2 = \min \frac{(-K[y], y)}{(M[y], y)}, \quad y \in S, \tag{4.1}$$

over a given function space S. A similar method has been used in the context of constrained cylindrical interfaces by Bostwick & Steen (2010). Some details of the theory will be presented here, while a discussion of this classical approach can be found in many sources (e.g. Segel 1987).

Given n orthonormal basis functions $\psi_i(x)$, which span an approximation to the function space S, the variational problem is reduced to a set of linear algebraic equations from which the eigenvalues/vectors are computed. A solution is constructed as a linear combination of the orthonormal basis functions,

$$y(x) = \sum_{i=1}^{n} a_i \psi_i(x). \tag{4.2}$$

Equation (4.2) is applied to the functional (4.1) and minimized with respect to the coefficients a_i. The resulting set of linear equations is written as

$$-\lambda^2 \sum_{i=1}^{n} M_{ij} a_i = \sum_{i=1}^{n} K_{ij} a_i, \quad j = 1, 2, \ldots, \tag{4.3}$$

with

$$M_{ij} \equiv \int_{-1}^{1} M[\psi_i]\psi_j \,\mathrm{d}x, \quad K_{ij} \equiv \int_{-1}^{1} K[\psi_i]\psi_j \,\mathrm{d}x, \quad i, j = 1, 2, \ldots . \tag{4.4}$$

Equation (4.3) is solved using standard numerical techniques. Given an eigenvalue $\lambda^{2(p)}$ and eigenvector $a_i^{(p)}$, the corresponding eigenfunction is

$$y^{(p)}(x) = \sum_{i=1}^{n} a_i^{(p)} \psi_i(x). \tag{4.5}$$

4.2. *Constrained function space*

To use the Rayleigh–Ritz procedure on (3.7), a function space that satisfies (3.6) is constructed. To begin, consider a piecewise test function

$$f(x) = \begin{cases} f_1(x), & -1 \leqslant x \leqslant \zeta_1, \\ 0, & \zeta_1 \leqslant x \leqslant \zeta_2, \\ f_2(x), & \zeta_2 \leqslant x \leqslant 1, \end{cases} \tag{4.6}$$

subject to the following conditions:

$$\int_{-1}^{\zeta_1} f_1(x)\,\mathrm{d}x + \int_{\zeta_2}^{1} f_2(x)\,\mathrm{d}x = 0, \tag{4.7a}$$

$$f_1(\zeta_1) = 0, \tag{4.7b}$$

$$f_2(\zeta_2) = 0. \tag{4.7c}$$

By construction, the test function (4.6) satisfies (3.6*c*) and therefore the no-penetration condition (2.10*b*). The functions $f_1(x)$ and $f_2(x)$ are the deformations of the respective free surfaces and are independent, *except for coupling via the conservation-of-volume constraint* (4.7*a*). The perturbation is single-valued, which dictates that its amplitude must vanish on the boundaries of the spherical-belt constraint (4.7*b*) and (4.7*c*). To construct functions that satisfy (4.7), assume the free-surface perturbations take the form

$$f_1(x) = \sum_{k=0}^{N} b_k P_k(x), \quad f_2(x) = \sum_{k=0}^{N} c_k P_k(x). \tag{4.8}$$

Substitution of (4.8) into (4.7) gives

$$b_0 \int_{-1}^{\zeta_1} P_0\,\mathrm{d}x + \cdots + b_N \int_{-1}^{\zeta_1} P_N\,\mathrm{d}x + \cdots + c_N \int_{\zeta_2}^{1} P_N\,\mathrm{d}x = 0, \tag{4.9a}$$

$$b_0 P_0(\zeta_1) + b_1 P_1(\zeta_1) + \cdots + b_N P_N(\zeta_1) = 0, \tag{4.9b}$$

$$c_0 P_0(\zeta_2) + c_1 P_1(\zeta_2) + \cdots + c_N P_N(\zeta_2) = 0, \tag{4.9c}$$

which is a set of three algebraic equations on the coefficients b_k and c_k

$$\begin{bmatrix} \int_{-1}^{\zeta_1} P_0(x)\mathrm{d}x & \cdots & \int_{-1}^{\zeta_1} P_N(x)\mathrm{d}x & \int_{\zeta_2}^{1} P_0(x)\mathrm{d}x & \cdots & \int_{\zeta_2}^{1} P_N(x)\mathrm{d}x \\ P_0(\zeta_1) & \cdots & P_N(\zeta_1) & 0 & \cdots & 0 \\ 0 & \cdots & 0 & P_0(\zeta_2) & \cdots & P_N(\zeta_2) \end{bmatrix} \begin{bmatrix} \boldsymbol{b} \\ \boldsymbol{c} \end{bmatrix} = [\boldsymbol{0}]. \tag{4.10}$$

There are $2(N+1)-3 = 2N-1$ linearly independent coefficient vectors that solve (4.10) and equivalently $2N-1$ linearly independent basis functions $\xi_k(x)$ which solve (4.7). The set of linearly independent functions is made orthonormal using Gram–Schmidt orthogonalization and a computer algebra package. The orthonormal basis functions inherit the properties of the linearly independent basis functions, such as identically satisfying the boundary/integral conditions (3.6). Finally, a solution series, which spans the constrained function space, is constructed using the orthonormal basis functions $\psi_k(x)$ as

$$y(x) = \sum_{k=1}^{2N-1} a_k \psi_k(x). \tag{4.11}$$

Finite N means that the function space and resulting solutions are approximate. Nevertheless, for ease of reference, we shall refer to well-converged solutions (4.11) as 'exact'.

5. Results

The solution series (4.11) is used to reduce the operator (3.7), via a Rayleigh–Ritz procedure, to a standard algebraic eigenvalue problem. The eigenfrequencies/modes, as they depend upon ρ_e/ρ_i, ζ_1 and ζ_2, are then computed from (4.3). Setting $N = 7$ for computation shows relative eigenvalue convergence to within 0.1 % for the results presented here. Equivalently, 13 terms are used in the solution series (4.11) with a resolution of eight terms on each free surface.

The Legendre polynomials on $[-1, 1]$ are known to span a function space suitable for capturing the Rayleigh and Strani solutions of the operator equation (3.7). With two interfaces, one must be careful to construct the solutions from an appropriately generalized space. It is convenient to report our solutions (4.11) of (3.7), denoted EX, as a contrast to those obtained using different spaces (e.g. different bases). The solutions on different spaces may be thought of as different approximate solutions (e.g. different truncations) having restricted degrees of freedom. A most severe approximation restricts disturbances to spherical-cap interfaces (Theisen *et al.* 2007), henceforth referred to as T07. These have a single degree of freedom (per interface) and constitute a one-parameter family of shapes. Applying Newton's law to the centre of mass of two coupled spherical caps leads to a second-order ordinary differential equation for the motion. A different restriction (Bostwick & Steen 2009), possible when the spherical-belt width is limited to a circle of contact, restricts to smooth surfaces (continuous derivatives across the circle of contact), which we denote B09. This restriction, in effect, couples the contact angles across the circle of contact. We start by comparing EX to the continuous B09 solutions, which are a limiting case of EX, and then to the 'spherical-cap' T07 solutions, which are not a sub-case of EX. Finally, we motivate and construct a two-oscillator approximation of the exact problem where the two fully deformable interfaces are coupled linearly. The utility of this approximation is demonstrated.

5.1. *Pinned circle-of-contact ($\zeta_1 = \zeta_2$) approximation*

Bostwick & Steen (2009) solve the pinned circle-of-contact problem by assuming a single smooth free surface. Solutions necessarily have a continuous derivative across the circle of contact. Figure 2 plots the frequency λ^2 against pin location ζ_1 for $\rho_e/\rho_i = 0$. Only the top half of the sphere ($0 \leqslant \zeta_1 \leqslant 1$) need be plotted since the frequencies are symmetric with respect to the pin location, $\lambda_n^2(\zeta) = \lambda_n^2(-\zeta)$. The figure shows the B09 frequencies are always larger than the EX frequencies with equality achieved at local minima (cf. figure 2*b*). The values of the local minima correspond to the 'unconstrained' Rayleigh frequencies (1.1) with mode number n. These minima occur at the 'nodes' of the corresponding unconstrained mode shapes, referred to as

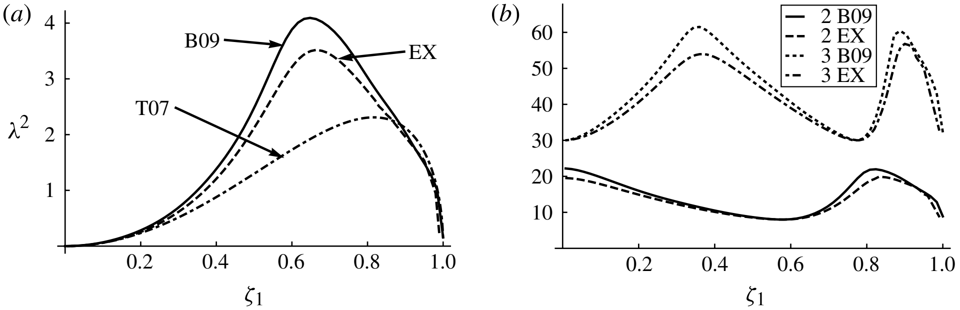

FIGURE 2. Frequency (λ^2) comparison between the discontinuous (EX), continuous (B09) (Bostwick & Steen 2009) and spherical-cap (T07) (Theisen *et al.* 2007) solutions for a drop pinned on a circle of contact ($\zeta_1 = \zeta_2$) with mode number: (*a*) $n = 1$; (*b*) $n = 2, 3$.

'natural' pin locations. As seen from the computed mode shapes of figure 3(*a,c*), the equator is a natural pin location for the odd mode shapes $n = 1, 3$. However, for even modes, the equator is an anti-node. These give local maxima of figure 2. Moreover, the EX modes exhibit discontinuous contact angles, disallowed by the B09 function space. For example, consider the $n = 2$ mode shape shown in figure 3(*b*). The conclusion is that the B09 function space is too narrow as a model of a droplet pinned at a contact circle. Recently, Prosperetti (2012) has solved the pinned circle-of-contact problem using expansions of the free surface and velocity potential in spherical harmonics. In this approach, the singularity in the curvature must be explicitly accounted for in cases where the derivative is not continuous. Prosperetti's frequencies are in excellent agreement with the EX frequencies.

5.2. *Spherical-cap approximation*

A different approximation (T07) arises when one restricts to centre-of-mass oscillations of a droplet pinned along a circle of contact (Theisen *et al.* 2007). T07 restrict to shapes that are pieces of spheres to analyse the dynamics of the centre of mass of two droplets coupled through a tube. In the limit of zero tube length, their problem is identical to ours. A snapshot of the corresponding experiments clearly shows that there are different contact angles across the constraint (Bostwick & Steen 2009, figure 10*a*). Figure 2(*a*) compares T07 with the $n = 1$ frequency from the B09 and EX solutions. The qualitative behaviour is similar. There is a single maximum and the frequency is zero at $\zeta_1 = 0$ and $\zeta_1 = 1$, but B09 most closely resembles the EX solution. B09 has uniformly higher frequencies, which can be directly attributed to the overly constrained function space. Note that differences between approximate and exact frequencies are exaggerated in the plot owing to the use of λ^2 as ordinate.

In general, the behaviour of the $n = 1$ EX mode shape, shown in figures 4(*a*) and 5(*a*), qualitatively resembles that of spherical-cap shapes and persists for finite-sized spherical-belt constraints. The flow induced by the $n = 1$ disturbance is relatively uniform, as evident from the streamlines plotted in figures 3(*d*)–5(*d*). In contrast, the $n > 1$ modes of figures 4 and 5 show richer behaviour, illustrating different ways that the two free surfaces communicate across the constraint. For example, the mode shapes of figures 4(*b,c*) and 5(*b*) appear to behave like a spherical-cap disturbance on one free surface and a higher-order shape on the other, which is consistent with qualitative experimental observations. This suggests that mode shapes may be excited where one free surface is relatively 'inactive' compared to the second free surface,

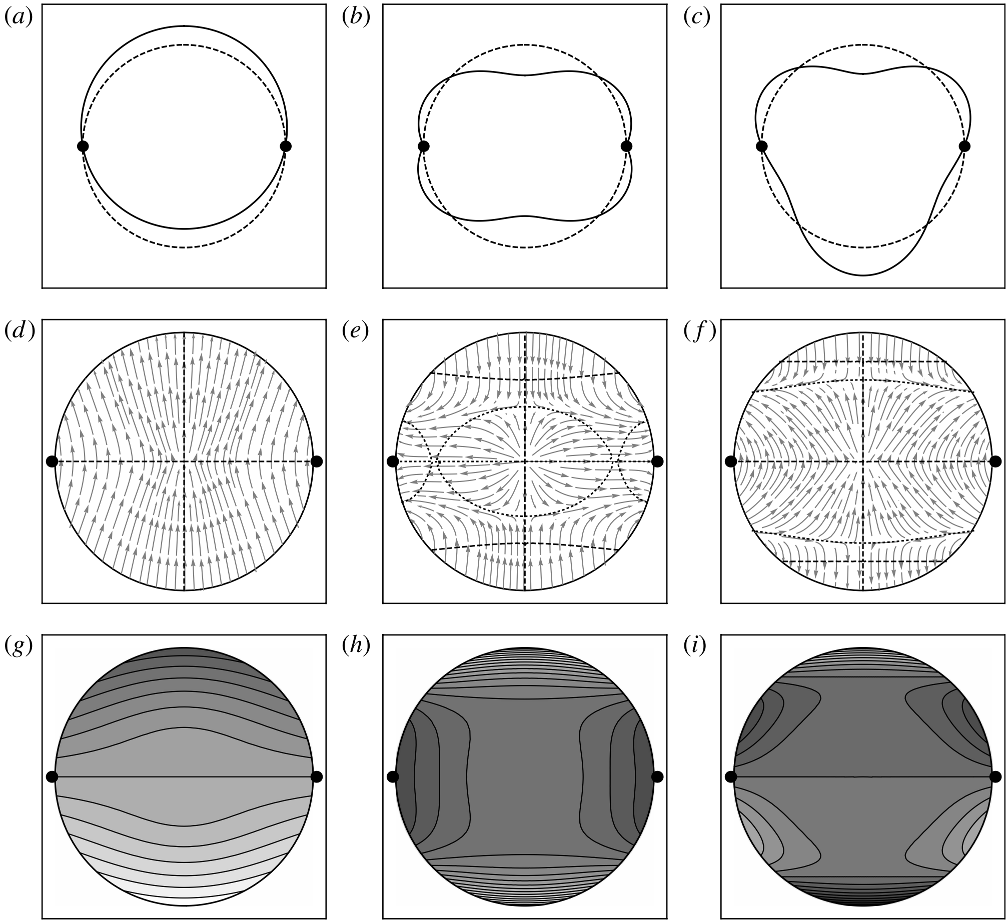

FIGURE 3. Eigenmodes (*a,d,g*) $n = 1$, (*b,e,h*) $n = 2$, and (*c,f,i*) $n = 3$, illustrating the (*a,b,c*) disturbed interface, (*d,e,f*) streamlines and (*g,h,i*) velocity potential (pressure) for a drop constrained by a pinned circle of contact at the equator ($\zeta_1 = \zeta_2 = 0$). Here the dashed (dotted) curves of (*d,e,f*) denote points of zero horizontal (vertical) velocity.

as exhibited by the velocity potential (pressure) shown in figure 4(*i*). Alternatively, figure 5(*c*) demonstrates that higher-order shapes can occur on both free surfaces. As the mode number n increases, the pressure fields are generally more localized around the free surfaces (cf. figures 3*h,i*–5*h,i*) and the flow becomes more complex (cf. figures 3*e,f*–5*e,f*). Lastly, we note that the pressure fields are relatively uniform within the fluid domain bounded by the spherical-belt support. Later, we shall use this observation in formulating the coupled-oscillator interpretation. For reference, figure 7 in Part 2 (Bostwick & Steen 2013) plots the mode shapes and streamlines for viscous motions using the same geometry as figure 4.

5.3. *Spectrum dependence on geometry*

Eigenfrequency is expected to increase with the extent of constraint based on experience with spectral problems. This expectation is realized in figure 6 where the first five frequencies are plotted as a function of the second pin location ζ_2, with

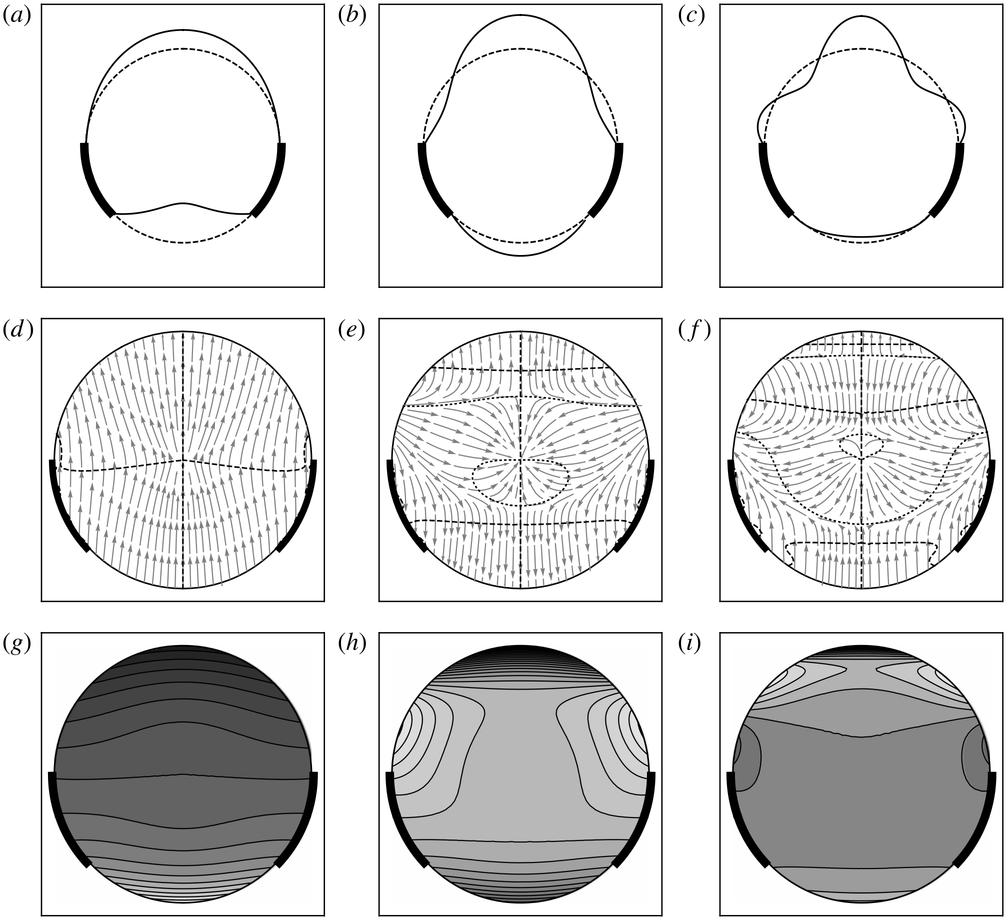

FIGURE 4. Eigenmodes (*a,d,g*) $n = 1$, (*b,e,h*) $n = 2$, and (*c,f,i*) $n = 3$, illustrating the (*a,b,c*) disturbed interface, (*d,e,f*) streamlines and (*g,h,i*) velocity potential (pressure) for a drop constrained by a spherical belt with $\zeta_1 = -0.7$, $\zeta_2 = 0$. Here the dashed (dotted) curves of (*d,e,f*) denote points of zero horizontal (vertical) velocity.

the first pin location ζ_1 held fixed ($\zeta_2 \geqslant \zeta_1 = 0.4$). Indeed, the frequency change is monotonic with constraint size but there are regions of slow and rapid growth. Slow growth is seen as a plateau or 'dead zone' over which an increase in belt size has no substantial influence on the frequency. Occasionally, in contrast, rapid growth occurs over a small increase in constraint extent.

In the dead zones, no appreciable change in mode shape is observed. For example, figure 7(*a,b*) shows only a slight variation in the mode shape between points A and B despite an eight-fold increase in constraint size (0.4/0.05). On the other hand, from C to D (cf. figure 7*c,d*), by counting the number of nodes on that surface, the mode shape of the ζ_1 surface (below) changes from $n = 2$ (C) to $n = 3$(D). The 'Strani oscillator limit', defined by $\zeta_2 \rightarrow 1$ in figure 6, corresponds to asymptotic lines of constant λ^2 whose numerical value is given by the corresponding eigenfrequency for the Strani oscillator of size $1 - \zeta_1$. A distinguishing feature of these asymptotes is that they connect dead zones of different mode numbers. For example, as seen in figure 6,

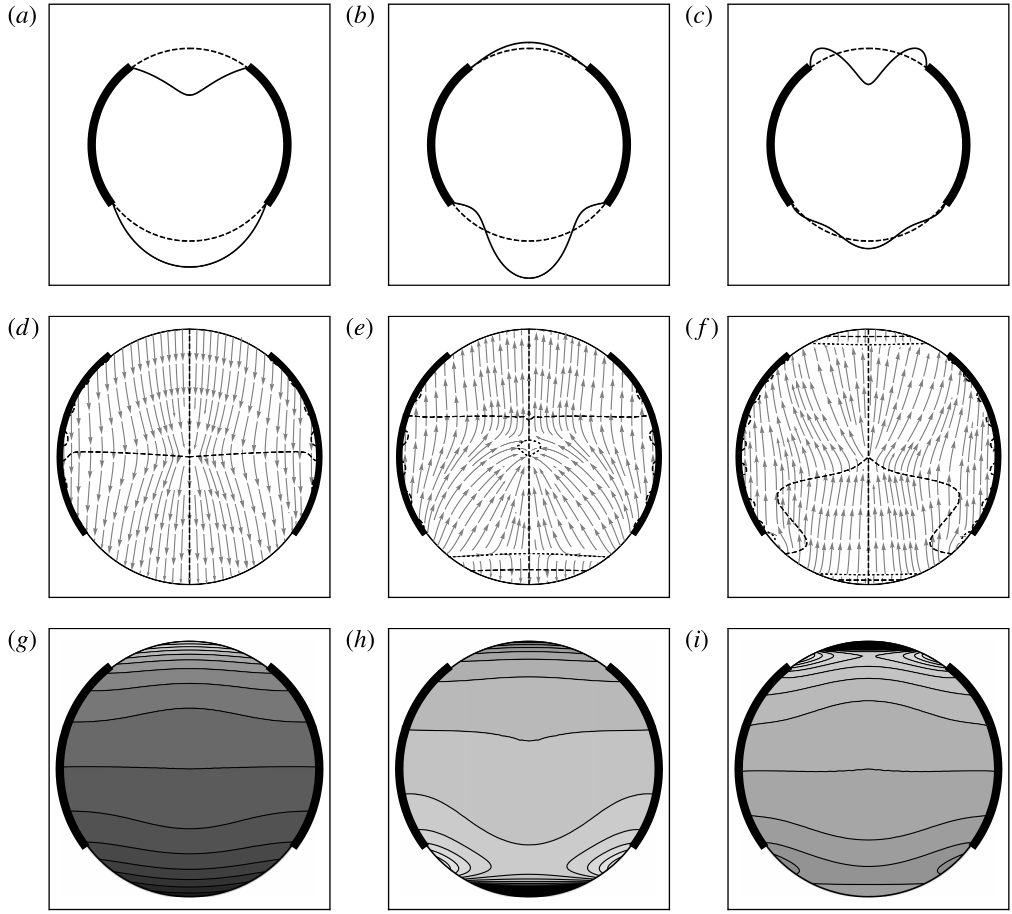

FIGURE 5. Eigenmodes (*a,d,g*) $n = 1$, (*b,e,h*) $n = 2$, and (*c,f,i*) $n = 3$, illustrating the (*a,b,c*) disturbed interface, (*d,e,f*) streamlines and (*g,h,i*) velocity potential (pressure) for a drop constrained by a spherical belt with $\zeta_1 = -0.6$, $\zeta_2 = 0.8$. Here the dashed (dotted) curves of (*d,e,f*) denote points of zero horizontal (vertical) velocity.

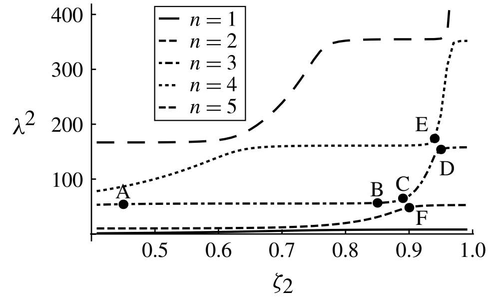

FIGURE 6. Frequency λ^2 against second pin location ζ_2 for fixed $\zeta_1 = 0.4$, which shows regions of slow ('dead') (A → B) and rapid (C → D) growth as the size of spherical-belt constraint increases, as well as the 'pinch points' between the $n = 2, 3$ (C, F) and $n = 3, 4$ (D, E) curves.

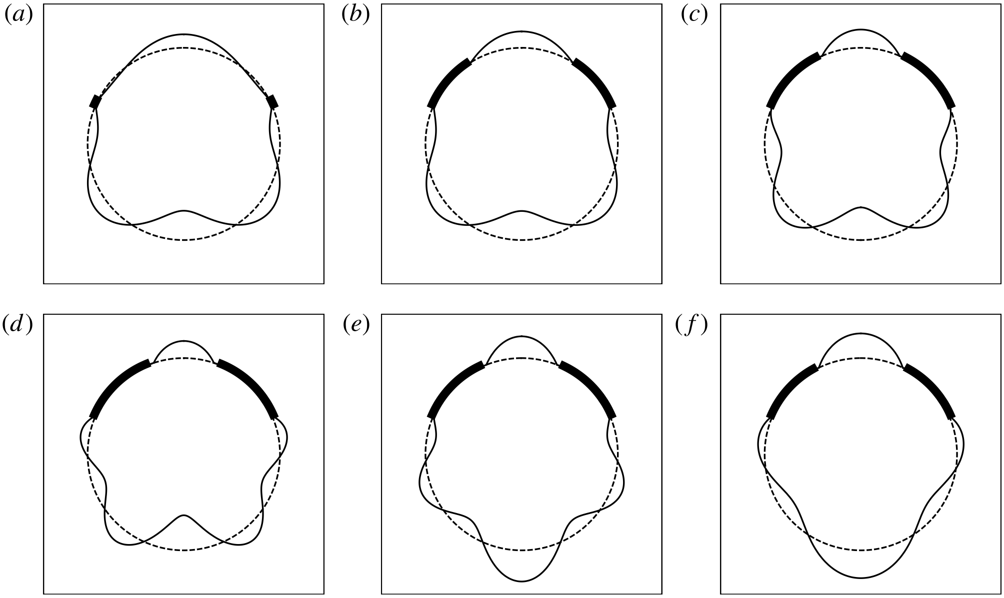

FIGURE 7. Mode shapes at: (*a*) point A ($\zeta_1 = 0.4, \zeta_2 = 0.45$); (*b*) point B ($\zeta_1 = 0.4, \zeta_2 = 0.85$); (*c*) point C ($\zeta_1 = 0.4, \zeta_2 = 0.9$); (*d*) point D ($\zeta_1 = 0.4, \zeta_2 = 0.95$); (*e*) point E ($\zeta_1 = 0.4, \zeta_2 = 0.95$); and (*f*) point F ($\zeta_1 = 0.4, \zeta_2 = 0.9$) of figure 6.

the dead zone between A and B has frequency corresponding to the Strani mode $n = 2$, even though it may have three nodal points (shape A). Note also that more than one dead zone may appear for fixed n, as seen along the $n = 5$ curve.

The dead zones can be understood as suppression of nodes. As seen in the progression from shape A to B to D in figure 7(*a,b,d*), one node shifts from the top surface (A) to the bottom surface (D). Over the dead zone (AB), the constraint suppresses that node. That is, the $n = 3$ mode shape varies little over the dead zone. Stated differently, over the dead zone one geometry differs little from the next.

5.4. *Algebraic and geometric identifications: the nodal index*

A spectral problem whose domain geometry has parametric dependence often exhibits ‘wavenumber selection’. For convective instabilities, for example, the geometry selects the wavenumber of the most unstable mode and certain cross-over geometries have two or more unstable modes (Charlson & Sani 1970; Beck 1972). In much the same way, for harmonics in free-surface problems, there can be cross-over geometries where two or more modes exhibit the same frequency or, in our case, nearly the same frequency. Before these results are presented, a short discussion concerning the algebraic/geometric identification of modes is necessary, as relevant to identifying modes in experiment.

For the Rayleigh problem, the frequency (algebraic) and shape (geometric) identities of modes coincide. That is, frequency ω_n in (1.1) corresponds to mode shape $P_n(\cos\theta)$ which exhibits n surface nodes on the half-circle. For the Strani oscillator, frequency of a mode and the count of surfaces nodes also coincide. In fact, modal labels are uniquely inherited from the Rayleigh problem by tracing back, i.e. via the limit $\zeta_1 \rightarrow 1$. In contrast, for our problem with two parameters, the path back to Rayleigh is

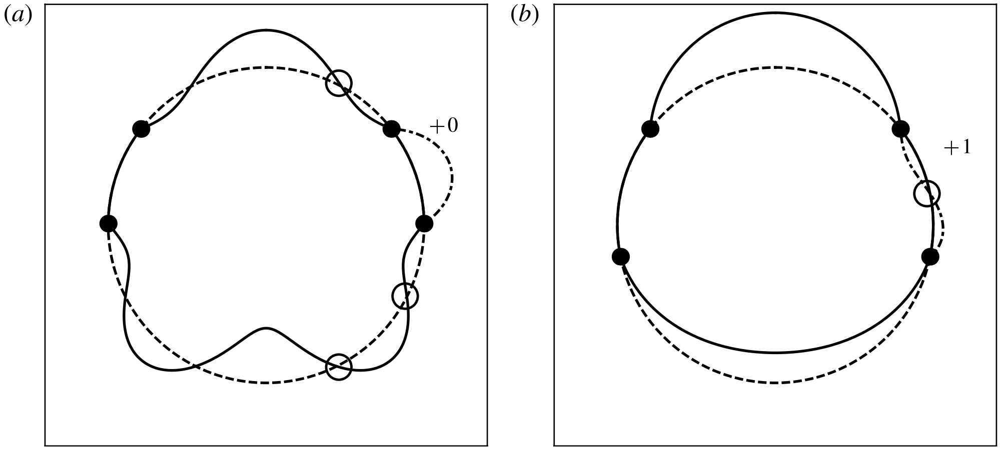

FIGURE 8. Nodal index n_i is defined by extending the disturbance to the full domain $0 \leqslant \theta \leqslant \pi$, illustrated for (*a*) a mode where $n_i = 3$, the same as the geometric index $n_g = 3$ obtained by counting nodes (circled) over both free surfaces. (*b*) Displays a mode where the nodal index $n_i = 1$ is one greater (circled) than the geometric index $n_g = 0$.

not unique and the labels are not conserved. Frequency and shape identities can differ. To illustrate, mode shapes A, B and D in figure 7(*a,b,d*) have algebraic identity $n = 3$ by association with eigenvalue λ_3. Stated differently, mode $n = 3$ has the third highest frequency in the spectral ordering over the entire range of ζ_2 constraint (figure 6). On the other hand, by counting the surface nodes on both surfaces one associates the geometric identity $n_g = 3$ for A, $n_g = 2$ for B and back to $n_g = 3$ for D. We call n_g the 'geometric index'. It gives the number of nodes one would observe in experiment.

It turns out that the geometric index n_g can be related to the algebraic index n. The idea is to imagine the disturbance as if on the Rayleigh-problem domain and ask what is the fewest number of nodes that must be added to have a smooth disturbance. The total count of nodes on this extension n_i, which we shall refer to as the 'nodal index', simply relates to the algebraic index n, $n_i = n$. The nodal index is illustrated on the completed domain for two different extensions in figure 8. In figure 8(*a*), the disturbance can be extended smoothly to the Rayleigh domain without adding a node. Thus, the nodal index $n_i = 3$ is identical to the geometric index $n_g = 3$. In contrast, for the disturbance shown in figure 8(*b*), at least one node must be added to have a smooth extended surface. Hence, the nodal index $n_i = 1$ is one greater than the geometric index $n_g = 0$. The nodal index for all three modes A, B and D, in figure 7(*a,b,d*) is $n_i = n = 3$. For reference, table 1 provides the index counts (n, n_g, n_i) for the modes shown in figure 7. In summary, the geometric index n_g can differ by one from the algebraic identity n, while the nodal index respects $n_i = n$.

5.5. *Multiplicity maps and the exchange volume*

Multiplicities in the solutions to the linear problem can occur at frequency 'crossings'. At these geometries, two different mode shapes have the same frequency. Near-multiplicities occur at near-crossings. For precisely locating near-crossings, however, a physically motivated alternative turns out also to be practical computationally.

Figure 7	Figure 6	n	n_g	n_i
a	A	3	3	3
b	B	3	2	3
c	C	3	2	3
d	D	3	3	3
e	E	4	3	4
f	F	2	2	2

TABLE 1. Algebraic (n), geometric (n_g) and nodal (n_i) index of the mode shapes shown in figure 7(*a–f*), which coincide with points A–F in figure 6.

Consider the volume displaced by the top surface, say, for a fixed eigenmode $y^{(n)}$,

$$V_n \equiv \int_{\zeta_2}^{1} y^{(n)}(x)\,\mathrm{d}x. \tag{5.1}$$

For a problem with only one interface, e.g. the Rayleigh or Strani drop, the volume displaced must be zero by volume conservation. With two or more interfaces, the volume displaced at any one interface must be absorbed at the other interfaces. Accordingly, the maximum interaction between any two specified interfaces occurs when the volumes displaced are the volumes exchanged. For two interfaces, volume displaced must equal the volume exchanged in magnitude. The volume exchanged can then be obtained by plotting volume displaced against constraint for various modes. It turns out that the crossings of these curves are an effective way to locate near-multiplicities of frequencies. For two interfaces volume exchanged must equal the magnitude of the displaced volume, of course. The volume exchanged then is obtained by plotting displaced volume against constraint for modes, pairwise, and locating crossings. It turns out that this is also an effective metric for locating near-multiplicities of frequencies.

The volume displaced V_n is plotted as a function of the second pin location ζ_2 while holding the first pin location ζ_1 fixed in figure 9(*c*,*d*). Volumes exchanged are identified by the notation D_{12} and D_{23} for the $n = 1$ and 2 modes and $n = 2$ and 3 modes, respectively. In contrast, the pinch points (points of closest approach) from figure 6 have been calculated and reproduced in figure 9(*a*,*b*). The pinch points are seen to coincide with the points of equal volume exchange, which justifies using the same notational labels for these. Note that the volume-exchange approach identifies near-multiplicities more precisely and unambiguously. The points $D_{n(n+1)}$ are transition points where the $n+1$ mode shape adds another node and becomes the primary volume carrier, taking volume from the n mode shape.

The physical interpretation of these crossings is that there is a change in the mode that dominates the response. This point is clarified in figure 10 which re-plots figure 6 with the crossing points labelled and connected by a best-fit curve. This best-fit curve turns out to be coincident with the curve obtained for a Strani-like oscillator (see discussion in § 5.6). It is thereby clear that, over the portions of the frequency curve connecting horizontal asymptotes, that is, over the active (non-dead) zones, the response is dominated by the smaller top surface to the extent that it is as if the other constraint were not present. On the other hand, over the dead zones, the response is dominated by the larger lower surface as the frequencies correspond to the $\zeta_2 \to 1$ asymptotes. The competition between constraints can be seen as a tug of war where

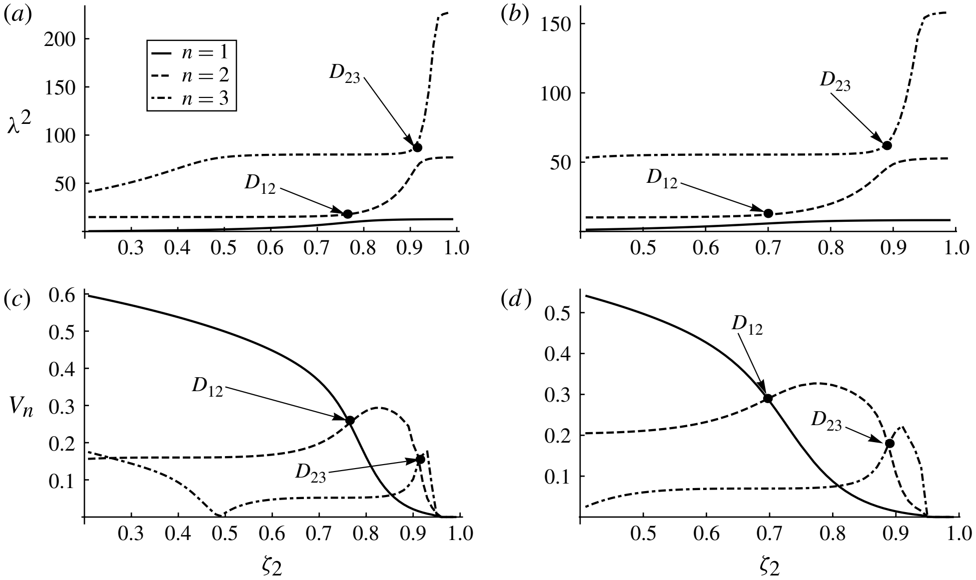

FIGURE 9. Location of the pinch points D_{ij} found by plotting (*a,b*) frequency λ^2 and (*c,d*) exchange volume V_n against second pin location ζ_2 for fixed (*a,c*) $\zeta_1 = 0.2$ and (*b,d*) $\zeta_1 = 0.4$.

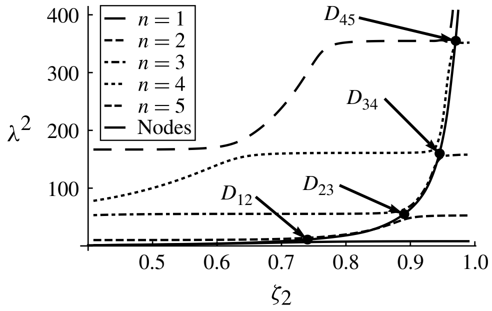

FIGURE 10. The node creation curve (labelled ‘Nodes’) made by connecting successive pinch points D_{ij} between the curves of frequency λ^2 against second pin location ζ_2 for fixed $\zeta_1 = 0.4$.

one constraint dominates and then the other as the combination of constraints shields the surface from the most active mode shapes. In summary, index n_g is conserved along the flat frequencies (horizontal lines) and jumps in n_g occur along the ascending frequencies curve.

A map of the geometric index n_g can also identify frequency crossings and is reported for the first four modes in figure 11. Only half of the constraint plane need be plotted by symmetry $\zeta_2 \geqslant \zeta_1$. At most two mode shapes have the same frequency. Crossings and near-multiplicities of frequencies occur along the boundaries in the map. The thickness of these boundary curves in the map of figure 11 reflect the accuracy of the boundary determination. For the lower harmonics, the locus of near-multiplicities tends to be smooth and the region where one mode dominates tends to be simply connected. For higher modes, cusps develop along the loci, cf. modes $n_g = 3$

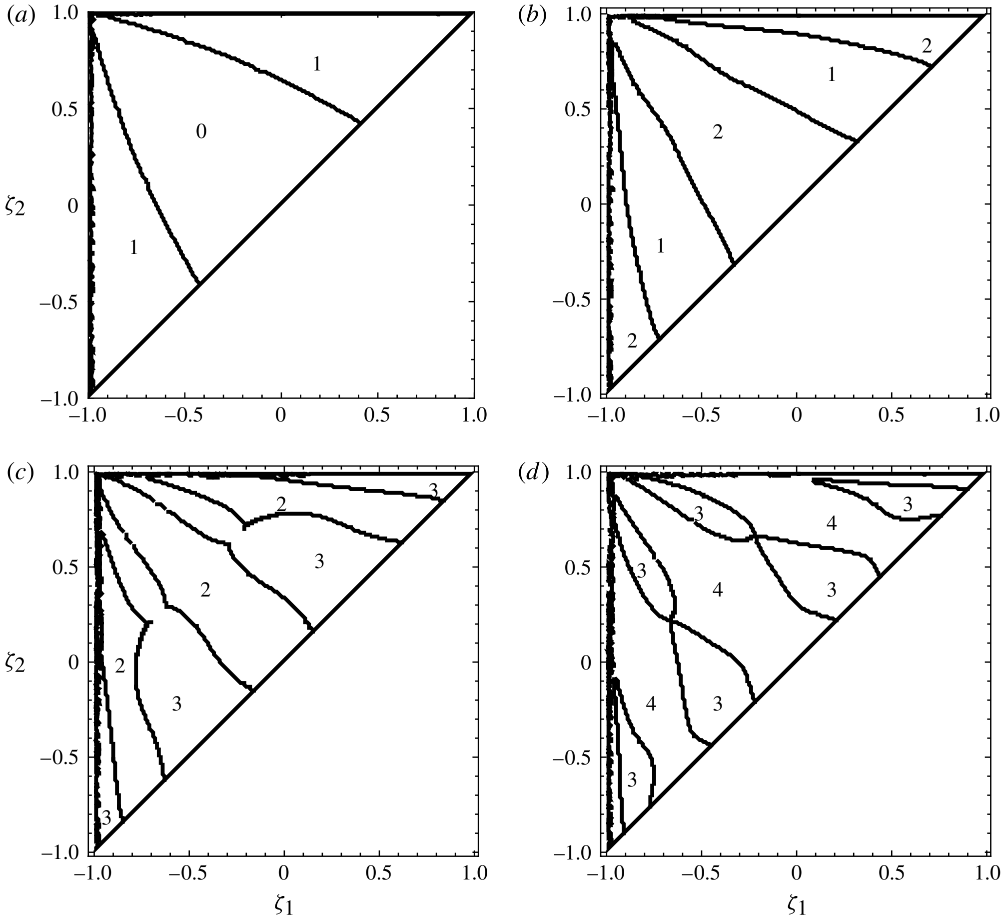

FIGURE 11. Multiplicity map gives geometric index n_g of lower harmonic (modes taken pairwise) as a function of pin location (ζ_1, ζ_2) for pairs: (*a*) the (dominant) lowest pair, $n_g = 0$ and $n_g = 1$ $(n = 1)$; (*b*) next lowest pair, $n_g = 1$ and $n_g = 2$ $(n = 2)$; (*c*) $n_g = 2$ and $n_g = 3$ $(n = 3)$; and (*d*) $n_g = 3$ and $n_g = 4$ $(n = 4)$. Boundary curve thickness reflects boundary uncertainty.

and $n_g = 4$, and regions are no longer simply connected. For constraints in the neighbourhood of the crossings, the system will be most sensitive and nonlinear interaction can be productively studied using tools such as weakly nonlinear analysis. These loci are also important from an engineering application viewpoint, as mentioned earlier.

5.6. *Coupled-oscillator approximation*

In the development above, the boundary conditions on the free surface $y(x)$ are applied in the final step of the procedure by incorporation into the function space (4.7). That is, the operator equation (3.7) is independent of pinning and volume-exchange constraints. In the previous section, we have seen how identifying the exchange volume aids in physical interpretation. In this section, we recast the problem to handle the volume exchange explicitly and show that this reformulation allows a reduction to coupled oscillators.

Consider the domain $-1 \leqslant x \leqslant 1$ split into the two free surfaces ∂D_1^f and ∂D_2^f as in the definition sketch $\partial D \equiv \partial D_1^f \cup \partial D_2^f \cup \partial D^s$ (figure 1). Next, subject the two free surfaces to the following volume-exchange constraints:

$$\int_{\partial D_1^f} y_1 = C, \qquad \int_{\partial D_2^f} y_2 = -C. \tag{5.2}$$

The displaced volume C is exchanged between the interfaces, preserving the total volume. By introducing Lagrange multipliers μ_1, μ_2, these constraints can now be shifted to the operator equation (3.7) through the introduction of the disturbance energy (augmented energy functional), as defined in the Introduction of Part 2 (Bostwick & Steen 2013),

$$\begin{aligned} F[y_1, y_2; \mu_1, \mu_2] = & \int_{\partial D_1^f} (\lambda_1 M[y_1] + K[y_1] + \mu_1) y_1 \\ & + \int_{\partial D_2^f} (\lambda_2 M[y_2] + K[y_2] + \mu_2) y_2. \end{aligned} \tag{5.3}$$

Here $\lambda_1 \equiv \sqrt{\rho_i \omega_1^2 R^3/\sigma}$ and $\lambda_2 \equiv \sqrt{\rho_i \omega_2^2 R^3/\sigma}$ are the oscillation frequencies (eigenvalues) of the associated free surface, to be determined. The integrals of (5.3) represent the respective disturbance energies of two 'Strani-like' oscillators, which are distinguished from the 'Strani' oscillator by the terms involving μ_1, μ_2. We justify the functional form of (5.3) by noting that, subject to a continuity condition on the surface of support, one can independently vary the free-surface disturbances y_1, y_2. That is, disturbances to oscillator 2, y_2, do not explicitly affect the disturbance energy of oscillator 1.

As stated earlier, the disturbance energy (4.1) is related to the operator equation (3.7); stationary values of the disturbance energy (4.1) necessarily satisfy the operator equation (3.7). Once again, recall that the operator equation (3.7) represents the balance of pressure at the free surface (functions), which is different from the disturbance energy (4.1), a scalar quantity. With regard to the augmented functional (5.3), stationary values of the disturbance energy satisfy the following two operator equations:

$$\lambda_1 M[y_1] + K[y_1] + \mu_1 = 0, \tag{5.4a}$$

$$\lambda_2 M[y_2] + K[y_2] + \mu_2 = 0. \tag{5.4b}$$

The Lagrange multipliers μ_1, μ_2 may now be interpreted physically as the constant pressure applied at each respective interface, required to displace a volume C. Thus, the difference between the 'Strani' and 'Strani-like' oscillator is the constant pressure term $\mu_{1,2}$ related to the coupling from the volume-exchange constraint (5.2). Equations (5.4*a*) and (5.4*b*) represent the balance of pressure at the free surface of oscillator 1 and 2, subject to the constant pressure μ_1 and μ_2, respectively. By this means, one can associate the operator equations (5.4) with two coupled Strani-like oscillators, where the coupling occurs through the pressures μ_1 and μ_2 which each depend on the other oscillator, in a way to be made explicit below.

We eliminate the Lagrange multipliers μ_1, μ_2 in favour of the displaced volume C by integrating the operator equations (5.4) over the respective undisturbed free surface and then enforcing the constraint (5.2) (i.e. embedding the displaced volume). The following reduced operator equations result:

$$\lambda_1 m_1[y_1; C] + k_1[y_1] = 0, \tag{5.5a}$$

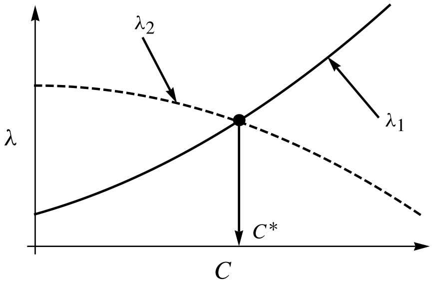

FIGURE 12. Illustration of free-surface frequencies λ_1 and λ_2 intersecting at a critical exchange volume C^*.

$$\lambda_2 m_2[y_2; C] + k_2[y_2] = 0. \tag{5.5b}$$

Here, we have rewritten the equations in a form reminiscent of two separate oscillators, each with effective spring constants

$$k_i[y_i] \equiv K[y_i] - \frac{\displaystyle\int_{\partial D_i^f} M^{-1}[K[y_i]]}{\displaystyle\int_{\partial D_i^f} M^{-1}[1]}, \quad i = 1, 2, \tag{5.6}$$

and effective mass, parameterized by C,

$$m_1[y_1; C] \equiv M[y_1] - \frac{C}{\displaystyle\int_{\partial D_1^f} M^{-1}[1]}, \quad m_2[y_2; C] \equiv M[y_2] + \frac{C}{\displaystyle\int_{\partial D_2^f} M^{-1}[1]}. \tag{5.7}$$

We have chosen to include the coupling in the effective mass term. Alternatively, it could be left to appear by itself on the right-hand side of the system, as in (5.4).

The solution strategy is now evident. Pick an exchange volume C, solve the operator equations (5.5) for the oscillation frequencies $\lambda_1(C), \lambda_2(C)$, and then impose the coupling through the fluid domain, which requires the frequencies to be in phase, $\lambda = \lambda_1(C^*) = \lambda_2(C^*)$, and which picks out a critical displaced volume C^*. In this final step, the determination of C^* requires the simultaneous solution of two scalar equations, schematically illustrated in figure 12. Accordingly, each mode shape exchanges a characteristic displaced volume C^* between disjoint free surfaces. As reported above, by making the displaced volume explicit, eigenvalue near-multiplicities are easily identified.

In summary, the displaced volume C can be viewed as a measure of 'communication' between free surfaces. A non-trivial displaced volume implies the disjoint surfaces are in communication, while mode shapes with zero volume exchange are essentially de-coupled. Furthermore, introducing the exchange volume allows the operator equation to be approximated as two coupled Strani-like oscillators. Thus, solution of the coupled oscillator problem (5.5) can be used to approximate the exact solution of (3.7). Should a reduction to a coupled-oscillator system be desired, any solution can be post-processed to identify effective mass (5.7) and spring (5.6) 'constants'.

6. Concluding remarks

The linear oscillations of an inviscid fluid drop, held by surface tension and constrained by a spherical belt are considered here. The integro-differential equation governing the interface deformation is formulated as an eigenvalue problem on linear operators. A solution is generated using the variational procedure of Rayleigh–Ritz on a constrained function space. To construct the constrained function space, we define the interface as the union of the two free surfaces and one surface of support and restrict 'allowable' solutions.

The free-surface deformations are independent and allowed to communicate, or exchange volume, across the surface of support, with coupling coming from the conservation-of-volume constraint. Across the pinned circle-of-contact constraint, allowable solutions must have a continuous interface but with discontinuous derivative (contact angle), in contrast to Bostwick & Steen (2009) where the single interface assumption requires the derivative also be continuous. As with the vibrating membrane and plate problems of classical mathematical physics (Courant & Hilbert 1953, Chap. 6), the more constrained the function space, the higher the frequency for comparable function spaces. Spherical-cap models have different degrees of freedom (different function spaces) and thereby can have higher or lower frequencies than the exact solution obtained here.

The dependence of frequency on the constraint geometry (ζ_1, ζ_2) is obtained. Dead zones and active zones are identified. The observed number of nodes n_g is seen to be conserved along dead zones with nodes introduced/removed along the active zones. Near-multiplicities of frequency occur near the intersection of dead and active zones. The near-multiplicities are marked by near-crossings in the frequency–geometry plot. It is observed that volume exchange is an effective metric for identifying the near-resonances. In the harmonic hierarchy, the geometric index n_g changes depending on constraint position and extent. Modal dominance (pairwise) is presented as a map over the (ζ_1, ζ_2) plane, where boundaries between regions in this plane represent geometries with near-resonances. The traditional node count n_g to identify mode shapes is ambiguous for the two-interface problem. This bookkeeping issue is resolved by introducing the nodal index n_i, simply related to the geometric index n_g, by which $n_g = n_i$ or $n_g = n_i - 1$, and for which $n_i = n$, the algebraic index.

In the final section of the paper, displaced volume is used again but as a measure of the communication between disjoint free surfaces. The volume constraint is shifted from the function space back to the equations using Lagrange multipliers. This leads to an approximation that couples two 'Strani-like' oscillators. Solutions to these equations can be post-processed to identify effective mass and spring constants, showing how to make precise a relationship to coupled oscillators.

Acknowledgements

This work was supported by NSF Grant CBET-0653831 and NASA Grant NNX09AI83G. The authors thank Dr A. Prosperetti for providing a preprint of Prosperetti (2012), wherein frequencies compare favourably to the curve EX in figure 2(*a*).

Note added in proof

Ramalingam, Ramkrishna & Basaran (2012), which first came to the authors attention while Parts 1 and 2 were under final review, redoes the B09 problem allowing for non-smooth surfaces at pin locations. Their figure 8 compares B09 to their EX and further confirms our figure 2(*a,b*).

REFERENCES

ARFKEN, G. B. & WEBER, H. J. 2001 *Mathematical Methods for Physicists*. Harcourt Academic Press.

BASARAN, O. & DEPAOLI, D. 1994 Nonlinear oscillations of pendant drops. *Phys. Fluids* **6**, 2923–2943.

BAUER, H. F. & CHIBA, M. 2004 Oscillations of captured spherical drop of frictionless liquid. *J. Sound Vib.* **274**, 725–746.

BAUER, H. F. & CHIBA, M. 2005 Oscillations of captured spherical drop of viscous liquid. *J. Sound Vib.* **285**, 51–71.

BECK, J. L. 1972 Convection in a box of porous material saturated with fluid. *Phys. Fluids* **15**, 1377–1383.

BHANDAR, A. S. & STEEN, P. H. 2005 Liquid-bridge mediated droplet switch: a tristable capillary system. *Phys. Fluids* **17**, 127107.

BISCH, C., LASEK, A. & RODOT, H. 1982 Compartement hydrodynamique de volumes liquides spheriques semi-libres en apesanteur simulee. *J. Mec. Theor. Appl.* **1**, 165–184.

BOSTWICK, J. B. & STEEN, P. H. 2009 Capillary oscillations of a constrained liquid drop. *Phys. Fluids* **21**, 032108.

BOSTWICK, J. B. & STEEN, P. H. 2010 Stability of constrained cylindrical interfaces and the torus lift of Plateau-Rayleigh. *J. Fluid Mech.* **647**, 201–219.

BOSTWICK, J. B. & STEEN, P. H. 2013 Coupled oscillations of deformable spherical-cap droplets. Part 2. Viscous motions. *J. Fluid Mech* **714**, 336–360.

BRUNET, P., EGGERS, J. & DEEGAN, R. D. 2009 Motion of a drop driven by substrate vibrations. *Eur. Phys. J. Special Topics* **166**, 11–14.

CHARLSON, G. S & SANI, R. L 1970 Thermoconvective instability in a bounded cylindrical fluid layer. *Intl. J. Heat Mass Transfe* **13**, 1479–1496.

COURANT, R. & HILBERT, D. 1953 *Methods of Mathematical Physics*, Vol. I. Wiley-Interscience.

DANIEL, S., SIRCAR, S., GLIEM, J. & CHAUDHURY, M. K. 2004 Racheting motion of liquid drops on gradient surfaces. *Langmuir* **20**, 4085–4092.

DEPAOLI, W. D., FENG, J. Q., BASARAN, O. A. & SCOTT, T. C. 1995 Hysteresis in forced oscillations of pendant drops. *Phys. Fluids* **7**, 1181–1183.

FAYZRAKHMANOVA, I. S. & STRAUBE, A. V. 2009 Stick-slip dynamics of an oscillated sessile drop. *Phys. Fluids* **21**, 072104.

GAÑAN, A. & BARERRO, A. 1990 Free oscillations of liquid captive drops. *Microgravity Sci. Technol.* **3**, 70–86.

HAMMACK, J. L. & HENDERSON, D. M. 1993 Resonant interactions among surface water waves. *Annu. Rev. Fluid Mech.* **25**, 55–97.

HIRSA, A. H., LOPEZ, C. A., LAYTIN, M. A., VOGEL, M. J. & STEEN, P. H. 2005 Low-dissipation capillary switches at small scales. *Appl. Phys. Lett.* **86**, 014106.

JAMES, A., SMITH, M. K. & GLEZER, A. 2003*a* Vibration-induced drop atomization and the numerical simulation of low-frequency single-droplet ejection. *J. Fluid Mech.* **476**, 29–62.

JAMES, A., VUKASINOVIC, B., SMITH, M. K. & GLEZER, A. 2003*b* Vibration-induced drop atomization and bursting. *J. Fluid Mech.* **476**, 1–28.

LOPEZ, C. A. & HIRSA, A. H. 2008 Fast focusing using a pinned-contact liquid lens. *Nat. Photonics 2* **9**, 610–613.

LOPEZ, C. A., LEE, C. C. & HIRSA, A. H. 2005 Electrochemically activated adaptive liquid lens. *Appl. Phys. Lett.* **87**, 134102.

LYUBIMOV, D. V., LYUBIMOVA, T. P. & SHKLYAEV, S. V. 2004 Non-axisymmetric oscillations of a hemispheric drop. *Fluid Dyn.* **39**, 851–862.

LYUBIMOV, D. V., LYUBIMOVA, T. P. & SHKLYAEV, S. V. 2006 Behavior of a drop on an oscillating solid plate. *Phys. Fluids* **18**, 012101.

MALOUIN, B. A., VOGEL, M. J. & HIRSA, A. H. 2010 Electromagnetic control of coupled droplets. *Appl. Phys. Lett.* **96**, 214104.

NOBLIN, X., BUGUIN, A. & BROCHARD-WYART, F. 2004 Vibrated sessile drops: transition between pinned and mobile contact lines. *Eur. Phys. J.* E **14**, 395–404.

NOBLIN, X., BUGUIN, A. & BROCHARD-WYART, F. 2005 Triplon modes of puddles. *Phys. Rev. Lett.* **94**, 166102.

NOBLIN, X., KOFMAN, R. & CELESTINI, F. 2009 Ratchet-like motion of a shaken drop. *Phys. Rev. Lett.* **19**, 194504.

OLLES, J. D., VOGEL, M. J., MALOUIN, B. A. & HIRSA, A. H. 2011 Axisymmetric oscillation modes of a double droplet system. *Optics Express* **19**, 19399–19406.

PROSPERETTI, A 2012 Linear oscillations of constrained drops, bubbles and plane liquid surfaces. *Phys. Fluids* **24**, 032109.

RAMALINGAM, S. K. & BASARAN, O. A. 2010 Axisymmetric oscillation modes of a double droplet system. *Phys. Fluids* **22**, 112111.

RAMALINGAM, S., RAMKRISHNA, D. & BASARAN, O. A. 2012 Free vibrations of a spherical drop constrained at an azimuth. *Phys. Fluids* **24** (8), 082102.

RAYLEIGH, LORD 1879 On the capillary phenomenon of jets. *Proc. R. Soc. Lond.* **29**, 71–97.

RODOT, H. A. & BISCH, C. 1984 Oscillations de volumes liquides semi-libres en microgravite-experience es326 dans spacelab 1. *5th European Symp. on Material Sciences under Microgravity, Paper* ESA SP-222, pp. 23–29.

SEGEL, L. A. 1987 *Mathematics Applied to Continuum Mechanics*. Dover.

STRANI, M. & SABETTA, F. 1984 Free vibrations of a drop in partial contact with a solid support. *J. Fluid Mech.* **141**, 233–247.

STRANI, M. & SABETTA, F. 1988 Viscous oscillations of a supported drop in an immiscible fluid. *J. Fluid Mech.* **189**, 397–421.

THEISEN, E. A., VOGEL, M. J., HIRSA, C. A., LOPEZ, A. H. & STEEN, P. H. 2007 Capillary dynamics of coupled spherical-cap droplets. *J. Fluid Mech.* **580**, 495–505.

TRINH, E. & WANG, T. G. 1982 Large-amplitude free and driven drop-shape oscillation: experimental results. *J. Fluid Mech.* **122**, 315–338.

TRINH, E., ZWERN, A. & WANG, T. G. 1982 An experimental study of small-amplitude drop oscillations in immiscible liquid system. *J. Fluid Mech.* **115**, 453–474.

TSAMOPOULOS, J. A. & BROWN, R. A. 1983 Nonlinear oscillations of inviscid drops and bubbles. *J. Fluid Mech.* **127**, 519–537.

VOGEL, M. J., EHRHARD, P. & STEEN, P. H. 2005 The electroosmotic droplet switch: Countering capillarity with electrokinetics. *Proc. Natl Acad. Sci.* **102**, 11974–1979.

VOGEL, M. J. & STEEN, P. H. 2010 Capillarity-based switchable adhesion. *Proc. Natl Acad. Sci.* **107**, 3377–3381.

VUKASINOVIC, B., SMITH, M. K. & GLEZER, A. 2007 Dynamics of a sessile drop in forced vibration. *J. Fluid Mech.* **587**, 395–423.

WANG, T. G., ANILKUMAR, A. V. & LEE, C. P. 1996 Oscillations of liquid drops: results from usml-1 experiments in space. *J. Fluid Mech.* **308**, 1–14.

WILKES, E. & BASARAN, O. 1999 Hysteretic response of supported drops during forced oscillations. *J. Fluid Mech.* **393**, 333–356.

WILKES, E. & BASARAN, O. 2001 Drop ejection from an oscillating rod. *J. Colloid Interface Sci.* **242**, 180–201.